Nonadiabatic quantum path analysis of the high-order harmonic generation in a highly ionized medium

2012 New J. Phys. 14 033009

(http://iopscience.iop.org/1367-2630/14/3/033009)

New Journal of Physics
The open-access journal for physics

Nonadiabatic quantum path analysis of the high-order harmonic generation in a highly ionized medium

Matteo Lucchini[1,3], Francesca Calegari[1], Kyungseung Kim[1,2], Giuseppe Sansone[1] and Mauro Nisoli[1,3]

[1] Department of Physics, Politecnico di Milano, National Research Council of Italy, Institute of Photonics and Nanotechnologies (CNR–IFN), Piazza L da Vinci 32, 20133 Milano, Italy
[2] Department of Physics and Coherent X-ray Research Center (CXRC), Korea Advanced Institute of Science and Technology (KAIST), Daejeon 305-701, Korea
E-mail: matteo.lucchini@mail.polimi.it and mauro.nisoli@fisi.polimi.it

New Journal of Physics **14** (2012) 033009 (13pp)
Received 3 October 2011
Published 9 March 2012
Online at http://www.njp.org/
doi:10.1088/1367-2630/14/3/033009

Abstract. The nonadiabatic saddle-point method is used to investigate the process of high-order harmonic generation in a gas, driven by few-optical-cycle pulses with above-saturation intensity and controlled electric field. The peculiar effects produced on the generation process by temporal reshaping of the driving field, induced by propagation in a highly ionized gas cell, can be used to control the electron quantum paths, which contribute to the harmonic generation process. It is shown that complete spectral tunability of the harmonic peak position over the entire extreme-ultraviolet spectrum, obtained by changing the carrier-envelope phase of the driving pulses, can be understood by considering the effects of driving pulse distortions on the phase of the relevant electron quantum paths.

[3] Author to whom any correspondence should be addressed.

Contents

1. Introduction 2
2. Theoretical model 3
3. Single-atom harmonic spectra: the role of propagation in the generation medium 6
4. Conclusions 12
Acknowledgments 13
References 13

1. Introduction

The production of extreme-ultraviolet (XUV) radiation by using the process of high-order harmonic generation (HHG) in a gas is by now a well-established method for the generation of ultrashort XUV pulses, with duration down to the attosecond temporal range [1], which has opened the way to a number of important applications, such as ultrafast spectroscopy in the XUV, high-resolution imaging, bio-microscopy, lithography and seeding of free-electron lasers (FELs). Moreover, it has been demonstrated that HHG provides a powerful way for reconstruction of the highest occupied molecular orbital (HOMO) in molecules [2]. The HHG process is understood in the framework of the semiclassical three-step model [3, 4]: the excitation of a gas medium with femtosecond light pulses with intensity of the order of 10^{13}–10^{15} W cm^{-2} leads to tunnel ionization of an atom or molecule; the liberated electron is then accelerated by the laser field and finally recombines with the parent ion, emitting excess energy in the form of high-energy photons. Various numerical methods, based on the strong-field approximation (SFA) [5], have been developed for the investigation of the physical processes at the basis of HHG. The nonadiabatic saddle-point (NASP) method has proven to be a powerful numerical technique, particularly in the case of few-optical-cycle driving pulses.

In the framework of the NASP method, the XUV generation process is described in terms of the complex trajectories (quantum paths) followed by the electrons from the ionization instant to recombination with the parent ion. Over the last few years, this numerical technique has been used for the investigation of various physical processes: (i) the role of the carrier-envelope phase (CEP) of few-cycle pulses on the short and long quantum paths in HHG [6, 7]; (ii) the polarization gating technique for the generation of isolated attosecond pulses [8, 9]; (iii) HHG in diatomic molecules [10]; (iv) terahertz-assisted HHG in atoms [11]; and (v) the CEP role of few-cycle driving pulses with above-saturation peak intensity in the ionization gating technique [12]. In the latter case, the sub-cycle ionization dynamics of the gas medium used for XUV generation is a crucial process, which strongly affects the temporal and spatial characteristics of both the XUV and the infrared (IR) pulses. Indeed, the propagation of high-intensity few-cycle pulses in an ionizing medium leads to distortion of the temporal evolution of the pulse electric field, which can strongly influence the XUV generation process [13–16].

We have experimentally demonstrated recently that the use of high-intensity driving pulses with few-optical-cycle duration and stable CEP offers the possibility to achieve complete spectral tunability of the harmonic peak position over the entire XUV spectrum, upon changing the CEP of the excitation pulse [17]. This behavior has been interpreted in terms of temporal reshaping of the electric field of the driving pulses in an ionizing gas, which offers the possibility to control the electron quantum paths contributing to HHG. We demonstrated that

such a quantum path control can be interpreted as a single-atom effect. In this work, we report on a detailed investigation of the single-atom response, obtained in the framework of the NASP method. In particular, we calculate the emission rates of the individual quantum paths as a function of the CEP of the driving pulse after propagation in a low-pressure gas cell. Moreover, we show that a careful analysis of the different contributions to the phase of the electron quantum paths leads to a simple physical interpretation of the observed tunability of the harmonic emission, in terms of plasma-induced chirp of the driving pulses. The paper is organized as follows. Section 2 contains a description of the theoretical method used in the paper and an investigation of the propagation effects on the driving field. After briefly recalling the main experimental result reported in [17], section 3 presents an analysis of the experimental data in terms of the NASP calculations. Finally, section 4 provides the conclusions.

2. Theoretical model

Using the saddle-point method, the Fourier transform of the single-atom dipole moment, $\mathbf{x}(\omega)$, can be written as a coherent superposition of various complex quantum paths, corresponding to the complex saddle-point solutions $(\mathbf{p}_s, t_s, t_s')$, where $\mathbf{p}_s$ is the stationary value of the electron momentum and t_s' and t_s are the ionization and recombination instants, respectively. Since in the case of high-intensity excitation, ground-state depletion cannot be neglected, $\mathbf{x}(\omega)$ can be written as [7]

$$\mathbf{x}(\omega) = \sum_s |\mathbf{x}_s(\omega)|\, e^{i\Theta_s(\omega)} \exp\left[-\int_{-\infty}^{\mathrm{Re}(t_s')} w(t'')\, dt''\right], \tag{1}$$

where $\mathbf{x}_s(\omega)$ is the contribution of the sth quantum path to the total single-atom spectrum, $\Theta_s(\omega)$ is the phase of the complex function $\mathbf{x}_s(\omega)$ and $w(t)$ is the tunnel ionization rate. We calculated $w(t)$ by using the Ammosov, Delone and Krainov (ADK) theory [18]. It is known that such a model could give an overestimation of the actual ionization rate when applied to intense and short pulses [19–21]. It is important to point out that, due to the very low gas pressure used in the experiments, the nature of the physical mechanism under investigation is not affected by the accuracy of the approximation adopted to calculate the ionization rate. Indeed, our choice is supported *a posteriori* by the excellent agreement between the calculations and the experimental results. The saddle-point equations can be written as a set of four equations for the real and imaginary parts of t_s' and t_s. It is quite simple to solve such a set of equations numerically if the driving electric field used in the calculations has an analytical form, i.e. if it is possible to know the value of the electric field for any complex time. In order to solve the saddle-point equations for electric fields with arbitrary temporal evolution, we have employed a modified version of the method reported by Kovács and Toşa [22]. In [22], the vector potential, $\mathbf{A}(t)$, and its integral, $\alpha(t) = \int_{-\infty}^{t} \mathbf{A}(t'')\, dt''$, are approximated in the complex domain by expanding them in a Taylor series around the real time values. This approximation is valid since $\mathrm{Im}(t_s) \ll \mathrm{Re}(t_s)$ and $\mathrm{Im}(t_s') \ll \mathrm{Re}(t_s')$ [23]. Taylor expansion requires us to calculate the numerical derivatives of the driving field. This operation could be nontrivial if high-order derivatives were required, since to overcome noise propagation through calculations could be difficult. We propose a different approach, easier to implement in a standard numerical computing environment. We have approximated $\mathbf{A}(t)$ and $\alpha(t)$ by making a polynomial fit of the two functions on the real

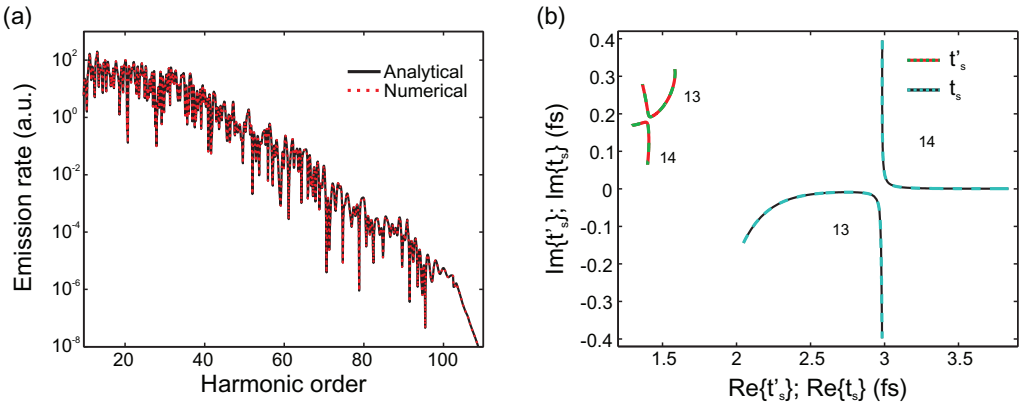

Figure 1. Results of the NASP calculations for driving electric field defined in an analytical (solid curves) and a numerical (dashed curves) way. (a) Single-atom emission rate; (b) imaginary and real parts of the ionization time t'_s and recombination time t_s for the 13th and 14th complex quantum paths. In this calculation, both long and short quantum paths are taken into account. The 13th trajectory (labelled by 13 in (b)) is the 7th *short* path; the 14th trajectory (labeled by 14 in (b)) is the 7th *long* quantum path (all the trajectories are ennumerated with increasing numbers starting from the first available short path). Parameters used in the calculation: electric field $E(t) = E_0 \cos^2(t/\tau)\cos(\omega_0 t + \psi)$; the laser central wavelength 750 nm; pulse duration 6 fs; pulse peak intensity 9×10^{14} W cm^{-2}; CEP $\psi = 0$; argon gas.

time axis and then exploiting the analytical extension of the polynomials:

$$A(t + i\zeta) \simeq \sum_n a_n (t + i\zeta)^n, \tag{2}$$

$$\alpha(t + i\zeta) \simeq \sum_n b_n (t + i\zeta)^n. \tag{3}$$

We tested the method assuming an input electric field with the analytical expression $E(t) = E_0 \cos^2(t/\tau)\cos(\omega_0 t + \psi)$. We have calculated the emission rates and the imaginary and real parts of the ionization and recombination times using the analytical expression of the electric field and its approximation. As shown in figure 1, the agreement between the two numerical procedures is excellent. Indeed, by using polynomials with degree n up to 30, we found that the relative difference between the two numerical procedures is confined to a value $<0.01\%$.

The propagation of the driving IR field in the gas cell was calculated by using a three-dimensional (3D) model, which solves the Maxwell equations for the IR in the framework of the slowly evolving wave approximation (SEWA) [24]. By using a coordinate frame that is moving at the group velocity v_g of the pulse and assuming radial symmetry, the driving electric field amplitude, $E(r, z, t)$, where z and r are the propagation and transverse coordinates, respectively, can be obtained by numerical solution of the following equation [25]:

$$\nabla^2 E(r, z, t) - \frac{1}{c^2}\frac{\partial^2 E(r, z, t)}{\partial t^2} = \frac{1}{\epsilon_0 c^2}\frac{\partial^2 P(r, z, t)}{\partial t^2}, \tag{4}$$

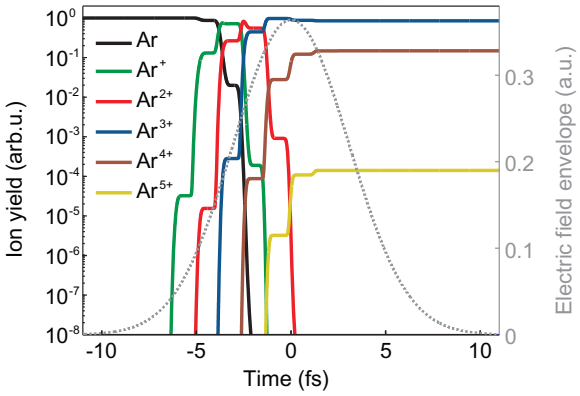

Figure 2. Calculated argon ion populations calculated at the input of the gas cell. Parameters used in the calculation: pulse duration 5 fs; pulse central wavelength 750 nm; pulse peak intensity 3.5×10^{15} W cm^{-2}; CEP $\psi = 0$.

where $P(r, z, t)$ is the polarization response of the medium and c is the vacuum velocity of light. Since the pressure used in the experiments and assumed in the numerical simulations is very low (3 torr), it is possible to neglect the loss of driving light energy due to ionization. In this case the second time derivative of the polarization is given by [25]

$$\frac{\partial^2 P(r, z, t)}{\partial t^2} \simeq \frac{e^2}{m_e} n_e(r, z, t) E(r, z, t), \tag{5}$$

where n_e is the electron density and e and m_e are the electron charge and mass, respectively. Therefore, equation (4) can be written as follows [26]:

$$\nabla^2 E(r, z, t) - \frac{1}{c^2} \frac{\partial^2 E(r, z, t)}{\partial t^2} = \frac{\omega_p^2(r, z, t)}{c^2} E(r, z, t), \tag{6}$$

where $\omega_p = [e^2 n_e(r, z, t)/\varepsilon_0 m_e]^{1/2}$ is the plasma frequency. This equation takes into account both temporal plasma-induced phase modulation and spatial plasma lensing effects, while it does not consider the linear gas dispersion and absorption of the driving beam, which are negligible under our conditions. This equation is then solved in the framework of the SEWA, which is applicable since the electric field changes along a propagation distance equal to the wavelength, λ, of the driving field are small (i.e. $|\partial E/\partial z| \ll E/\lambda$). As pointed out in [24], the SEWA requires that not only the envelope of the electric field, but also the CEP do not significantly change over a propagation distance equal to λ, so that it does not impose a limitation on the pulse duration. Moreover, the electric field is assumed to be slowly varying in the transverse dimensions at a distance comparable to λ (i.e. $|\partial E/\partial r| \ll E/\lambda$).

The electron density, n_e, was calculated using the ADK model in a nonadiabatic way. The contribution to the total electron density coming from multiple ionization, induced by the high excitation intensity, is calculated by applying the ADK in sequence. Figure 2 shows, as a dotted line, the temporal evolution of the electric field envelope of a 5 fs pulse (full-width at half-maximum (FWHM)) with the central wavelength of 750 nm and the calculated ion yield in the case of argon, assuming an excitation peak intensity $I = 3.5 \times 10^{15}$ W cm^{-2} and a pulse CEP $\psi = 0$. Due to the high intensity, multiple-charge ions, Ar^{n+}, are generated with n up to 5. Neutral atom, Ar^+ and Ar^{2+} populations are completely depleted on the leading edge of the pulse, so that the electron density is strongly affected by multiple ionization.

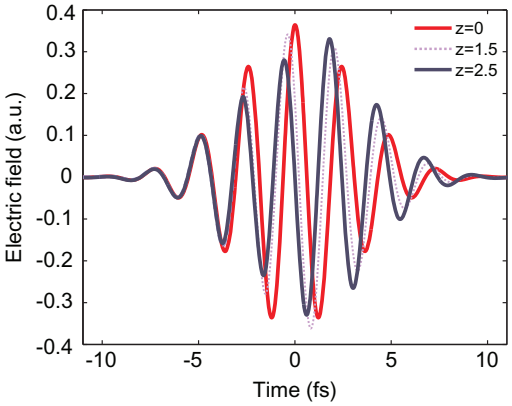

Figure 3. Electric field of a 5 fs driving pulse for three different positions inside a gas cell containing argon at a pressure $p = 3$ torr. Parameters used in the calculation: pulse central wavelength 750 nm; pulse peak intensity 3.5×10^{15} W cm^{-2}; CEP $\psi = 0$.

We then calculated the evolution of the electric field of the linearly polarized, 5 fs driving pulse along propagation in a cell containing argon at a static pressure $p = 3$ torr. We assumed a laser beam with a truncated-Bessel spatial profile, which corresponds to the fundamental EH_{11} hybrid mode of the hollow fiber used for pulse compression [27, 28]. The temporal evolution of the electric field at the input of the cell ($z = 0$) was $E(t) = A_0 \cos(\omega_0 t + \psi) \exp(-t^2/2\tau^2)$. Figure 3 shows the calculated electric field (assuming $r = 0$) for three different z positions in the gas cell. The temporal evolution of the electric field is significantly affected by propagation in the ionizing medium. While pulse duration is only slightly influenced, as shown by dashed lines in figure 4, which display the electric field envelope, the propagation induces a strong chirp on the leading edge of the pulse. Already after a propagation of 1.5 mm (see figure 4(b)), the instantaneous frequency, $\omega_0(t)$ (defined as the first derivative of the laser field temporal phase), is no longer constant and displays a complex peaked evolution in a temporal window between -5 fs and 0 fs (red dotted curve). Such complex behavior can be simply understood in terms of the refractive index change induced by the temporal variation of the electron density, $\partial n_e/\partial t$. Indeed, the time-dependent frequency modulation can be calculated as [29]

$$\delta\omega_0 = \frac{e^2 z}{2\pi m_e \omega_0 c} \frac{\partial n_e}{\partial t}. \tag{7}$$

Since the ionization rate strongly changes when the driving field presents an amplitude maximum, we expect to observe an increase in the instantaneous frequency for time values close to the maxima of the electric field, as indeed shown in figures 4(b) and (c): the instantaneous frequency displays clear peaks in correspondence to the local maxima of $\partial n_e/\partial t$.

3. Single-atom harmonic spectra: the role of propagation in the generation medium

We recently reported on the generation of tunable XUV radiation by using high-intensity, few-cycle driving pulses [17]. Harmonic generation has been achieved by focusing 5 fs IR pulses (peak intensity $I = 3.5 \times 10^{15}$ W cm^{-2}) in a 2.5 mm long cell filled with argon at low static pressure (2.5–3 torr). The gas cell was placed after the laser focus, so that short quantum paths predominantly contribute to the XUV generation [30, 31]. A 200 μm diameter pinhole was

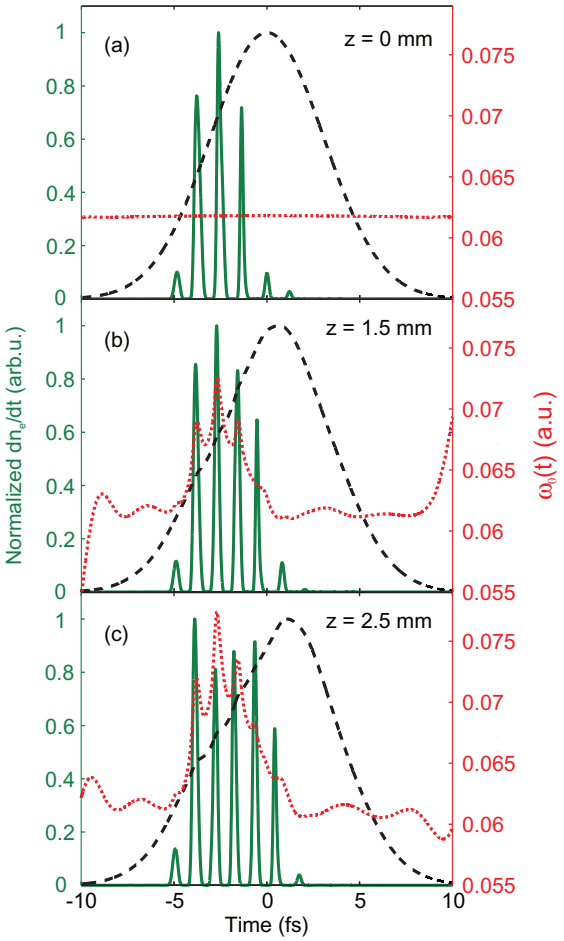

Figure 4. Field envelope (black dashed line), instantaneous frequency (red dotted line) and derivative of the electron population (green line) for (a) $z = 0$ mm, (b) $z = 1.5$ mm and (c) $z = 2.5$ mm.

positioned in the XUV-beam path in order to select only the on-axis radiation with homogeneous characteristics (details can be found in [12]). Figure 5 displays the measured harmonic spectra for five different CEP values, showing complete spectral tunability of the harmonic peaks over the entire spectral range.

In order to obtain a clear physical picture of the observed tunability, we have used the NASP method to calculate the contributions of electron quantum paths to the XUV generation process. As a result of the very low gas pressure used in the experiment, the calculated spatial reshaping of the driving pulse turns out to be rather weak. Due to the selection of the on-axis XUV components obtained by the use of the spatial filter on the XUV beam, in the NASP calculations we have considered the on-axis ($r = 0$) electric field, whose temporal evolution is shown in figure 3. Figures 6(a)–(c) show the XUV atomic spectra calculated for various CEP values of the driving field in a range of 3π, at three different positions inside the gas cell. Figures 6(d)–(f) show the corresponding harmonic emission rates associated with the relevant short quantum paths for two CEP values. The short quantum paths are labelled with increasing numbers starting from the first available complex trajectory. The spectral characteristics of the harmonic emission strongly depend on the position inside the gas cell, i.e. on the particular temporal evolution

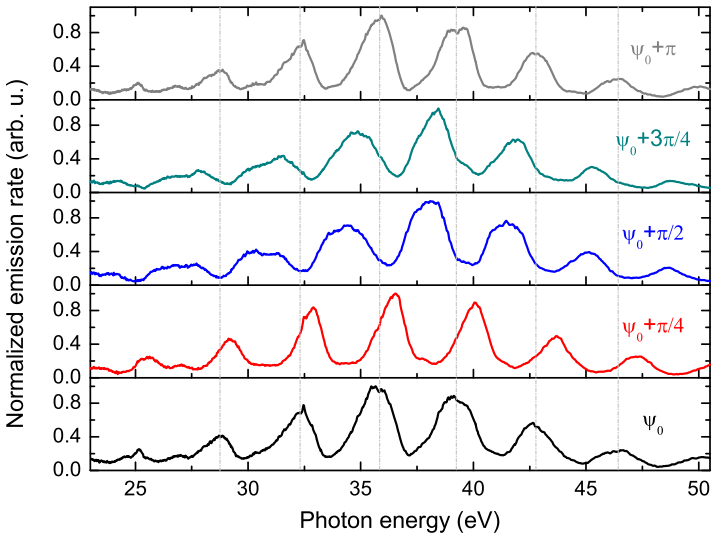

Figure 5. Experimental XUV spectra generated in a 2.5 mm thick argon cell by 5 fs pulses with $3.3 \pm 0.3 \times 10^{15}$ W cm^{-2} peak intensity and five CEP values separated by $\pi/4$.

of the driving electric field. At the input of the cell, $z = 0$, the XUV spectra show a periodic evolution upon changing the CEP by π. The harmonic peak position is negligibly affected by CEP; only in the cutoff region (photon energies larger than ~50 eV) the peak position is CEP dependent (as has already been observed in the case of few-cycle driving pulses [32, 33]). As shown in figure 6(d), for particular CEP values only one short path dominates thus giving a more continuous spectrum. Upon changing the CEP by $\pi/2$ the total emission rate is predominantly generated by two quantum paths (paths 3 and 4), which give similar contributions. In the case of $z = 1.5$ mm, a clear dependence of the harmonic peak position versus CEP is obtained in the entire spectral range (see figure 6(b)). Also in this case, the main contribution to the total emission rate is due to quantum paths 3 and 4, but their CEP dependence is changed. At the output of the gas cell ($z = 2.5$ mm) the emission rates of the third and fourth short quantum paths get closer in absolute value. Even for this z-position, the major contributions to the total emission rate originate from the third and fourth quantum paths. Indeed, the less steep leading edge of the driving pulse (see figure 4(c)) causes ground-state population depletion to occur later in time. Thus, the contribution of the fifth short quantum path becomes more relevant even if its emission rate is always at least two orders of magnitude smaller than the XUV spectra associated with complex trajectories 3 and 4 (figure 6(f)). As clearly shown in figure 6(c) and (i), at $z = 2.5$, the harmonic peak position shows complete tunability over the entire spectral range. This is in excellent agreement with the experimental results shown in figure 5. It is worth pointing out that at any position inside the cell, the total emission rate can be associated with only two recollision events, so that only two attosecond pulses are predominantly generated.

In the spirit of the NASP model, the single-atom harmonic emission rate, $W(\omega)$, can be written as

$$W(\omega) \simeq \omega^3 \, |\mathbf{x}(\omega)|^2 \simeq \omega^3 | \sum_s |\hat{\mathbf{x}}_s(\omega)| \, \mathrm{e}^{\mathrm{i}\Theta_s(\omega)}|^2, \tag{8}$$

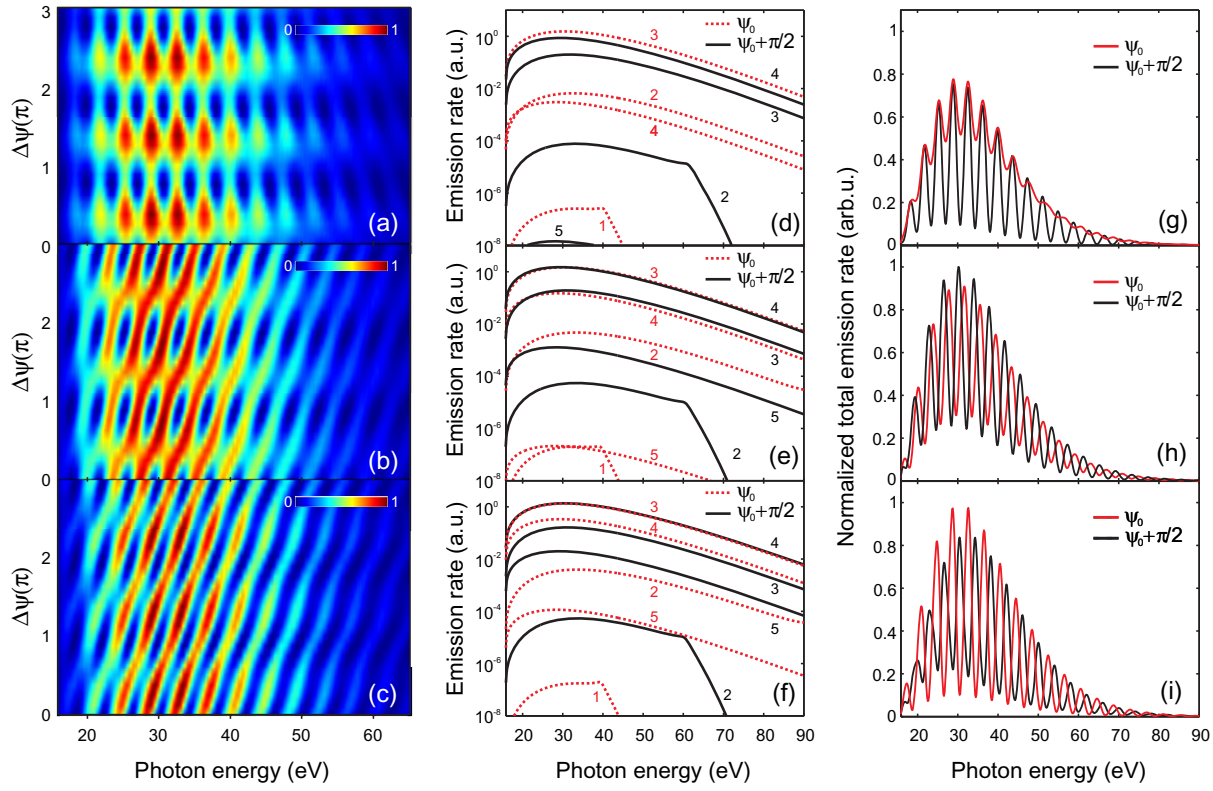

Figure 6. Calculated atomic XUV spectra as a function of the CEP ψ and the length of propagation distance z inside the generation cell: (a–c) single-atom emission as a function of the CEP at a z position inside the generation cell equal to 0, 1.5 and 2.5 mm, respectively; (d–f) emission rates of the short quantum trajectories for two CEP values ψ_0 and $\psi' = \psi_0 + \pi/2$; (g–i) harmonic emission rates for the two selected CEP values: ψ_0 (red line) and ψ' (black line). The same parameters as in figure 3.

where

$$\hat{\mathbf{x}}_s(\omega) = \mathbf{x}_s(\omega) \exp\left[- \int_{-\infty}^{\mathrm{Re}(t_s')} w(t'')\, \mathrm{d}t'' \right]. \tag{9}$$

Therefore, in the case under investigation, $W(\omega)$ can be approximated as

$$W(\omega) \simeq \omega^3 \Big| \sum_{s=3,4} |\hat{\mathbf{x}}_s(\omega)|\, \mathrm{e}^{\mathrm{i}\Theta_s(\omega)} \Big|^2. \tag{10}$$

The position of the harmonic peaks is determined by the condition of constructive interference between the relevant quantum paths:

$$\Delta\Theta(\omega) = \Theta_4(\omega) - \Theta_3(\omega) = 2m\pi \quad (m \in Z). \tag{11}$$

Figure 7 shows the calculated phase difference, $\Delta\Theta(\omega)$, at the input (figure 7(a)) and at the output (figure 7(b)) of the cell. At $z = 0$, $\Delta\Theta$ increases almost linearly with photon energy, with negligible dependence upon CEP, apart from a small deviation for the high-energy region of the spectrum [6]. The corresponding harmonic emission rates, calculated using equation (10) for

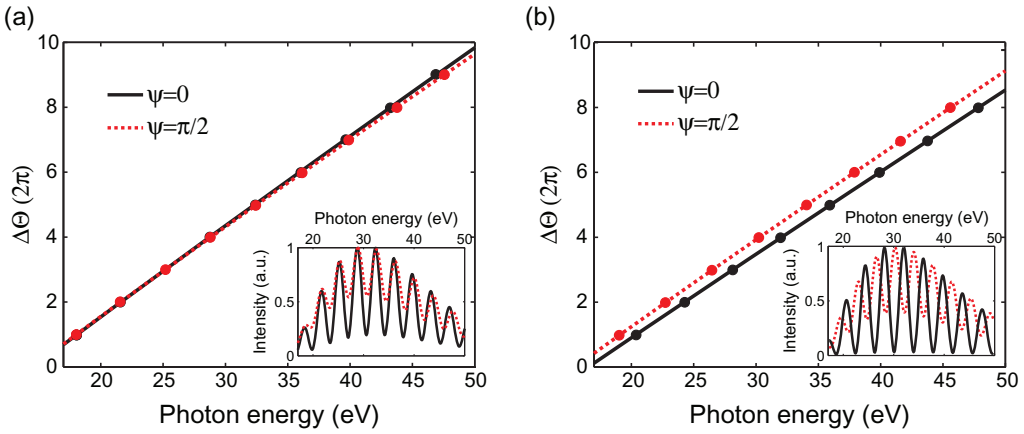

Figure 7. $\Delta\Theta$ in units of 2π calculated at $z = 0$ (a) and $z = 2.5$ mm (b) for two values of the pulse CEP ($\psi = 0$, black line; $\psi = \pi/2$, red line). The dots mark the points of constructive interference. The insets show the corresponding harmonic emission rate calculated by using equation (10).

two different CEP values and shown in the inset of figure 7(a), are characterized by harmonic peak positions almost insensitive to the CEP of the driving field, in agreement with the results obtained by considering the contributions of all the quantum paths (figures 6(a) and (g)). At the output of the gas cell, $\Delta\Theta$ shows a strong dependence on CEP. By changing the CEP value of $\pi/2$ the phase difference curve is clearly shifted. Therefore, the condition of constructive interference is obtained for different energy values and the corresponding harmonic peaks are out of phase, as displayed in the inset of figure 7(b), in agreement with the results obtained by considering the contributions of all the quantum paths (figures 6(c) and (i)).

The CEP effects on the quantum paths, giving rise to the tunability of the harmonic radiation, can be understood on taking into account the various contributions to the phase of each complex electron trajectory. The phase of the ith quantum path can be written as

$$\Theta_i(\omega) = \omega t_i - S_i(\omega) + \chi_i(\omega), \tag{12}$$

where the first term depends on the recombination time $t_i(\omega)$, the second is the stationary phase $S_i(\omega)$ and the third is a residual phase term, which turns out to be negligible compared to the previous two terms. Therefore, we will concentrate our attention on ωt_i and $S_i(\omega)$. In particular, the first can be decomposed into two contributions, which depend on the ionization time $t_i'(\omega)$ and the time spent by the free electron in the continuum, $\tau_i(\omega)$: $\omega t_i = \omega(t_i' + \tau_i)$. According to our analysis the phase difference between the third and the fourth short paths can then be written as

$$\Delta\Theta(\omega) = \omega\Delta t' + \omega\Delta\tau - \Delta S + \Delta\chi. \tag{13}$$

The role played by the various terms of equation (13) can be better analyzed by considering the difference between the quantity $\Delta\Theta$ calculated for two CEP values, ψ, which differ by $\pi/2$ ($\psi = 0$ and $\psi = \pi/2$):

$$\Delta\Theta_{0-\pi/2} = \Delta\Theta|_{\psi=0} - \Delta\Theta|_{\psi=\pi/2} = \omega\Delta t'_{0-\pi/2} + \omega\Delta\tau_{0-\pi/2} - \Delta S_{0-\pi/2} + \Delta\chi_{0-\pi/2}, \tag{14}$$

where $\Delta\chi_{0-\pi/2} \approx 0$. The results are shown in figure 8, at the input of the gas cell ($z = 0$, solid curves) and at the output of the cell ($z = 2.5$ mm, dashed curves). At $z = 0$, $\Delta\Theta_{0-\pi/2}$ (black solid

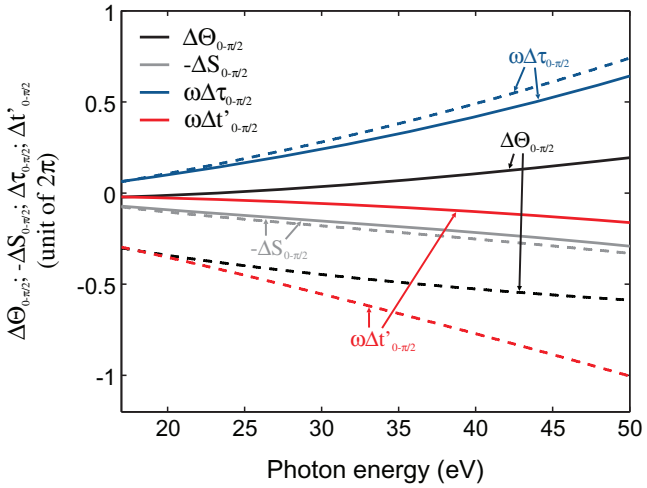

Figure 8. $\Delta\Theta_{0-\pi/2}$, $-\Delta S_{0-\pi/2}$, $\omega\Delta\tau_{0-\pi/2}$ and $\omega\Delta t'_{0-\pi/2}$ in units of 2π calculated at $z = 0$ (solid curves) and $z = 2.5$ mm (dashed curves).

curve in figure 8) slowly increases from zero on increasing the photon energy; in the spectral region where most of the harmonic energy is contained, $\Delta\Theta_{0-\pi/2}$ does not exceed $\pi/5$. In this case, the phase difference term depending on the time spent in the continuum, $\omega\Delta\tau_{0-\pi/2}$, is always positive, in the energy range of the figure, while the phase difference terms $-\Delta S_{0-\pi/2}$ and $\omega\Delta t'_{0-\pi/2}$ have negative values, and almost compensate for the positive term, at least in the low photon energy region; in the cutoff region the total phase difference is dominated by the term $\omega\Delta\tau_{0-\pi/2}$. At the output of the gas cell (dashed curves in figure 8), the phase difference terms $-\Delta S_{0-\pi/2}$ and $\omega\Delta\tau_{0-\pi/2}$ are similar to the corresponding terms calculated for $z = 0$, while the term related to the ionization times, $\omega t'_{0-\pi/2}$, exhibits completely different behavior versus photon energy and dominates the total dephasing $\Delta\Theta_{0-\pi/2}$. Therefore, we can conclude that the shift with CEP of the $\Delta\Theta(\omega)$ curve at $z = 2.5$ mm (see figure 7(b)) can be understood in terms of a modification of the ionization times difference of the two relevant quantum paths, induced by propagation of the driving pulse in the ionizing medium.

From a physical point of view it is possible to show that the different behavior of $\Delta t'$ observed for different values of the propagation coordinate z is directly related to the plasma-induced chirp of the driving pulse. Indeed, it is well known that in the case of short quantum paths, a good estimation of the difference between the ionization times of two consecutive paths is the half-optical cycle: $T_0(t)/2 = \pi/\omega_0(t)$. Therefore, for a particular photon energy, it is possible to estimate $\Delta t'$ by calculating an average local value of $T_0(t)/2 = T_0^{\mathrm{av}}/2$, where T_0^{av} is defined as the inverse of the average value of the instantaneous frequency $\omega_0(t)$ between t'_3 and t'_4 (such a procedure is shown in figures 9(a) and (b)). Figure 9(c) shows $\Delta t'$ and $T_0^{\mathrm{av}}/2$ as a function of the CEP of the driving pulse, calculated for a particular photon energy (35 eV). In the case of $z = 0$, both $\Delta t'$ and $T_0^{\mathrm{av}}/2$ do not show a clear dependence on the CEP value. In contrast, in the case of $z = 2.5$ mm, $\Delta t'$ and $T_0^{\mathrm{av}}/2$ change in the same way as a function of CEP. The offset between the $\Delta t'$ and $T_0^{\mathrm{av}}/2$ curves in the case of $z = 0$, which decreases for $z = 2.5$ mm, can be easily explained. Indeed, for a fixed energy, $\Delta t'$ is equal to $T_0/2$ only if the driving field is monochromatic. The third and the fourth quantum paths are located on the leading edge of the driving pulse, so that they are affected by the strong nonadiabatic increase

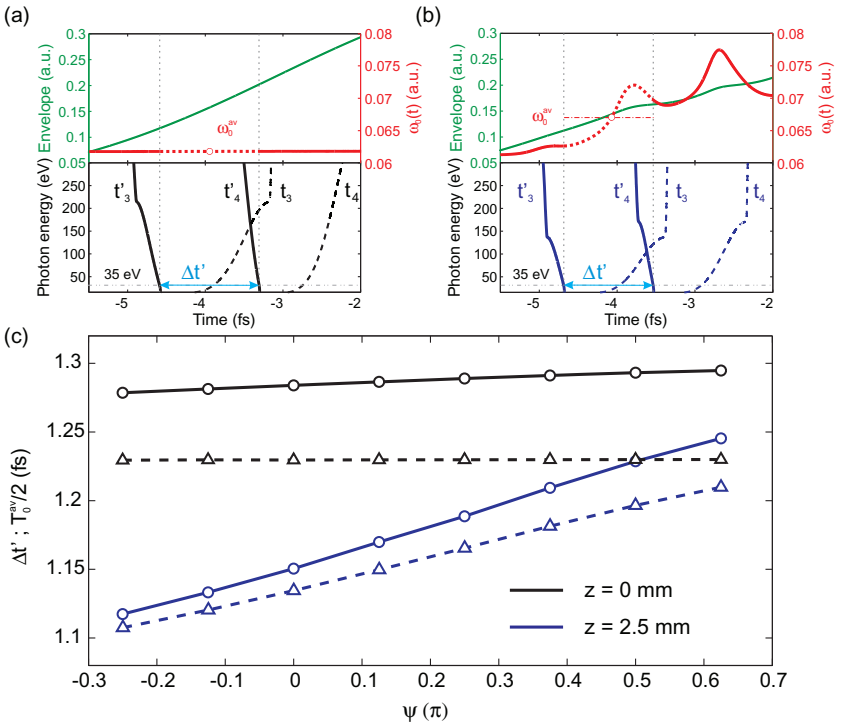

Figure 9. Comparison between the difference in the ionization times $\Delta t'$ and the average half-optical cycle $T_0^{\mathrm{av}}/2$. Panels (a) and (b) show the IR envelope (green line), $\omega_0(t)$ (red line), the ionization (solid black or blue lines) and recombination (dashed black or blue lines) times associated with the third and the fourth short trajectories calculated at $z = 0$ and $z = 2.5$ mm, respectively. The interval of ω_0 drawn with a dashed line marks the region in which the average is performed in order to obtain $T_0^{\mathrm{av}} = 2\pi/\omega_0^{\mathrm{av}}$. All quantities are evaluated at a CEP value $\psi = 0$. Figure (c) shows $\Delta t'$ (solid lines) and $T_0^{\mathrm{av}}/2$ (dashed lines) for a fixed photon energy value of 35 eV and different driving field CEP values ($z = 0$, black lines; $z = 2.5$ mm, blue lines).

of the electric field at the input of the gas cell. After the propagation in the ionizing medium the shape of the field changes and the rising edge becomes less steep (as shown by the green curves in figures 9(a) and (b)), thus reducing the nonadiabatic effect and consequently the offset between $\Delta t'$ and $T_0^{\mathrm{av}}/2$.

4. Conclusions

We have used the nonadiabatic saddle-point method, with ground-state depletion correction, for the theoretical investigation of the spectral properties of high-order harmonic radiation generated by high-intensity, few-optical-cycle pulses. The generation of tunable XUV radiation, by using few-optical cycle driving pulses with high intensity and controlled electric field, is understood in the framework of a single-atom approach. A simple numerical approximation is introduced to perform NASP calculations in the case of driving electric fields with arbitrary temporal evolution. By analyzing the phase terms of the relevant quantum paths, we demonstrated that only the term related to the electron ionization times turns out to induce

relevant effects on the observed CEP dependence of the XUV radiation. Finally, a simple model has been used, showing that the observed tunability can be understood in the framework of a single-atom model as a result of the plasma-induced chirp of the driving field. The nonadiabatic saddle point approach offers a powerful method for understanding the physical mechanisms involved in a number of strong-field phenomena induced by few-optical-cycle pulses and can be used as an effective guideline for a simple interpretation of the experimental results.

Acknowledgments

We thank S Stagira for useful discussions on the numerical model. We acknowledge funding from the European Research Council grant agreement 227355-ELYCHE; the Italian Ministry of Research (FIRB-IDEAS RBID08CRXK); and the European Union under contract 228334 JRA-ALADIN and MC-RTN ATTOFEL (FP7-238362).

References

[1] Corkum P B and Krausz F 2007 *Nature Phys.* **3** 381
[2] Itatani J *et al* 2004 *Nature* **432** 867
[3] Krause J L, Schafer K J and Kulander K C 1992 *Phys. Rev. Lett.* **68** 3535
[4] Corkum P B 1993 *Phys. Rev. Lett.* **71** 1994
[5] Lewenstein M, Balcou Ph, Ivanov M Yu, L'Huillier A and Corkum P B 1994 *Phys. Rev.* A **49** 2117
[6] Sansone G, Vozzi C, Stagira S and Nisoli M 2004 *Phys. Rev.* A **70** 013411
[7] Sansone G *et al* 2006 *Phys. Rev.* A **73** 053408
[8] Sansone G *et al* 2009 *Phys. Rev.* A **80** 063837
[9] Sansone G 2009 *Phys. Rev.* A **79** 053410
[10] Figuera de Morisson Faria C 2007 *Phys. Rev.* A **76** 043407
[11] Balogh E *et al* 2011 *Phys. Rev.* A **84** 023806
[12] Ferrari F *et al* 2010 *Nature Photonics* **4** 875–9
[13] Sekikawa T, Kosuge A, Kanai T and Watanabe S 2004 *Nature* **432** 605
[14] Kim K T, Kim C M, Baik M, Umesh G and Nam C H 2004 *Phys. Rev.* A **69** 051805
[15] Abel M *et al* 2009 *Chem. Phys.* **366** 9
[16] Cheng J *et al* 2011 *Phys. Rev.* A **84** 043411
[17] Calegari F *et al* 2011 *Phys. Rev.* A **84** 041802
[18] Ammosov M V, Delone N B and Krainov V P 1986 *Sov. Phys.—JETP* **64** 1191
[19] Vladimir S Popov 2004 *Phys.—Usp.* **47** 855
[20] Bauer D and Mulser P 1999 *Phys. Rev.* A **59** 569
[21] Tong X M and Lin C D 2005 *J. Phys. B: At. Mol. Opt. Phys.* **38** 2593
[22] Kovács K and Toşa V 2010 *J. Mod. Opt.* **57** 977–83
[23] Milošević D B, Becker W and Kopold R 2000 *Phys. Rev.* A **61** 063403
[24] Brabec T and Krausz F 1997 *Phys. Rev. Lett.* **78** 3282
[25] Geissler M *et al* 1999 *Phys. Rev. Lett.* **83** 2930
[26] Priori E *et al* 2000 *Phys. Rev.* A **61** 063801
[27] Marcatili E A J and Schmeltzer R A 1964 *Bell. Syst. Tech. J.* **43** 1783
[28] Nisoli M, De Silvestri S and Svelto O 1996 *Appl. Phys. Lett.* **68** 2793
[29] Miyazaki K and Takada H 1995 *Phys. Rev.* A **52** 3007
[30] Salières P, L'Huillier A and Lewenstein M 1995 *Phys. Rev. Lett.* **74** 3776
[31] Mairesse Y *et al* 2003 *Science* **302** 1540
[32] Baltuška A *et al* 2003 *Nature* **421** 611
[33] Nisoli M *et al* 2003 *Phys. Rev. Lett.* **91** 213905